Chapter 5
Building 3D Surface Model of the Human Hip Bone from 2D Radiographic Images Using Parameter-Based Approach

Milica Tufegdzic and Miroslav D. Trajanovic

5.1 Introduction

Human hip bone represents a very complex morphological structure of irregular shape, resulting from the fusion of three primarily stand-alone bones: ilium, ischium and pubic bone. Being a part of the skeletal system, the hip bone can be significantly damaged due to various traumas, tumors and other pathological conditions. Hip bone fractures are fractures of any constitutive bone, such as pubic fractures, partial fractures of the ischium and ilium bone or pubic dislocations which involve acetabulum. Some of these traumas require the use of osteofixation materials (reconstructive plates, fixators, screws, clamps). Tumor resections have to be conducted with great precision and are followed by bone reconstruction process, which requires the existence of some personalized prosthesis and implants. They are constructed to completely match the lost part of the bone after tumor removal. In such cases, having a high-quality 3D model of the bones is necessary in order to simulate the correct placement of osteofixation materials and implants in a virtual environment, and to plan and simulate the surgical procedure.

Direct procedures for creating 3D models of hip bone are almost impossible to apply due to complex bone shapes, as well as lack of explicit knowledge about surface shape. The procedures used to reconstruct the 3D geometric model of individual bones are based on free-form technologies with a certain degree of approximation and reverse engineering technologies. Initial data for reverse engineering procedures are obtained from volumetric medical images, mostly by using procedures like CT or Magnetic Resonance Imaging (MRI). These digital images have different resolutions

M. Tufegdzic (✉)
Department of Information Technology, Academy of Professional Studies Sumadija, Trstenik, Serbia
e-mail: mtufegdzic@asss.edu.rs

M. D. Trajanovic
Faculty of Mechanical Engineering, University of Nis, Nis, Serbia

O. Canciglieri Junior and M. D. Trajanovic (eds.), *Personalized Orthopedics*,
https://doi.org/10.1007/978-3-030-98279-9_5

and therefore consist of point clouds of different densities. These point clouds need to be converted into usable 3D geometric models that can be translated into a digital representation of a physical object in reverse engineering procedures.

3D polygonal models are used for visualization purposes in the cases when high accuracy of the model is not required, since they have a certain degree of approximation of rough surfaces. However, for planning and simulating operations, as well as in the processes of osteofixation materials design, and similar applications, it is necessary to have a quality 3D volume model. This requirement is particularly pronounced in production of personalized implants. 3D polygonal and volume hip bone models can be acquired by reverse engineering methods only if there is a sufficiently dense point cloud of complete bone. Otherwise, in the case of incomplete data, it is not possible to obtain high-quality 3D model and to conduct accurate patient-specific bone reconstruction. For such cases, a new method of parametric regions was developed, using information about specific anatomical points and parameters, which represent a prerequisite for complete morphometry of the hip bone. Parameter-based approach, with the aid of statistical tools, allows for determining regression models for predicting the position of points on the hip bone surface. These positions are used for creating a surface model of the hip bone and/or its parts in the cases when all available input data are taken from two biplanar X-ray projections. The resulting 3D surface point models of the wing of ilium bone and its part as examples, are accurate enough for application in systems for planning and simulation of operative flow, as well as creating 3D models of missing parts of bone for the purpose of making implants and constructing personalized osteofixation material and similar applications.

5.1.1 Methods for 3D Models Reconstruction

Statistical modeling and analysis of anatomical shapes is the subject of research in the field of medical images (Styner et al. 2003; Chintalapani et al. 2007). Statistical shape analysis is important for 3D reconstruction of anatomical structures and improvement of shape prediction from incomplete input, while multivariate statistical analysis helps to determine the relevant shape variation in the population (Aguirre et al. 2007).

The anatomical structures of different individuals show large but limited natural variability that can be statistically represented. Appropriate parametric description of surfaces is needed to preserve variability and given characteristics. In methods that use parametric description of surfaces, deformable super-quadratics can be used in combination with local deformation modeling, a series of extensions, or coordinates of points on the surface (Sierra et al. 2006).

Similar to the representation of surfaces of any object, 3D bone surface models can be presented in the form of meshes or Non-uniform Rational B-Splines (NURBS) (Su et al. 2013). It is also possible to represent the surface of an object (like the bone) with the set of unique points in 3D space which have the same positions on each

object (so-called "landmarks"). Each item belongs to a particular part of the object. Point Distribution Model (PDM) in 2D or 3D is obtained by statistical examination of the landmarks' positions (Zsemlye 2005). Nonlinear models such as polynomial regression point distribution model, are based on polynomial regression, where the variation modes in linear model are replaced by polynomial curves (Kirschner 2013). In order to simplify and reduce the number of parameters describing the 3D object, modal analysis can be used, with the help of Delaunay methods in the reconstruction process (Angelopoulou et al. 2015).

Finding correspondent points is essential for the automatic production of statistical surface models from an initial set of 3D surfaces. In order to solve the problem of point correspondence, minimum description length function can be used for error reduction and generalization (Zsemlye 2005; Kirschner 2013; Chen and Shapiro 2009). The iterative closest point method can be used to establish correspondences (Zsemlye 2005; Blanc et al. 2012).

Predicting the shape of a particular organ or its part in practice, especially in the case of incomplete surface shape information, is performed on the basis of various predictors, using three methods: Principal Component Analysis (PCA), which is also known as principal component regression, partial least squares and canonical correlation analysis. Scalar predictors, such as morphometric and anthropometric parameters, can be directly included in the aforementioned regression models (Blanc et al. 2012). Prediction techniques, based on observing the population, are used when shapes need to be predicted based on partial information. Minimizing the Mahalonobis distance is an iterative technique for shape prediction. The surface is controlled by selected points on the surface that the user can directly identify in a given data set. The positions of these landmarks represent the boundary conditions for shapes (Zsemlye 2005). Some parametric shape description methods use deformable superquadrics combined with local deformable modeling or point coordinates of the vertices of the surface. It is possible to reduce the number of parameters to a certain degree using procedures such as PCA (Sierra et al. 2006). Spherical harmonic description allows parametric shape description, where shapes can be represented by an object that has a spherical topology (Styner et al. 2003; Zsemlye 2005; Besbes 2010).

A great number of anatomical researches of the human hip bone were conducted with the aim of studying its morphology and morphological variations that depend on age, sex, characteristics of a certain population, etc. In some previous studies, 3D polygonal models of the human hip bone have been created in specialized programs for processing medical images or statistical models for estimating shapes and variations, but the applied methods give results only when there is a complete and high-quality volumetric image of the whole bone.

Lamecker et al. (2004) have created a statistical surface model for semi-automatic segmentation of the pelvic bone, based on its polygonal model (mesh). A statistical surface model was generated from 23 CT images of the male pelvic bones. Statistical shape and intensity models of the pelvic bone were generated from a set of initial polygonal models, specific for given patient, using the PCA method and by generating virtual X-rays from deformable anatomical models (Ehlke et al. 2013). Statistical

shape model was obtained from 50 CT scans which were manually segmented and converted into polygonal models (Seim et al. 2008). Statistical atlases of anatomical bone shapes from 110 CT images of individual patients were obtained using PCA and PDM, through procedures for identifying landmarks, establishing point-to-point correspondence and conducting statistical analysis to study shape variations (Chintalapani et al. 2007).

A hybrid method originating from combining incomplete data obtained from a CT image and geometric data from a visible human data set was used to generate the pelvis' finite element model, using higher-order Hermite cubic elements. Corresponding anatomical points were selected automatically from CT images, and the pelvic bone was divided into 4 regions (Shim et al. 2007). An anatomical model of the left half of the pelvic bone was constructed from input data in the form of a point cloud, obtained by a 3D laser scanner. Point cloud is further converted into triangle grid surface with certain assumptions and limitations (Phillips et al. 2007).

The hip bone is generated by a reverse engineering process through several steps. A high-precision replica was digitalized using a 3D laser scanner, resulting in a cloud of high-density dots. This initial point cloud was imported into the reverse engineering software, where the model was cleaned, after which the initial surface model was obtained (Popov and Onuh 2009). Surface model of female hip bone was obtained by reverse engineering in Computer Aided Design (CAD) software through following steps: data acquisition from CT scanner and pre-processing, creating an initial polygonal model, healing and smoothing, identification and defining the anatomical and morphological characteristics which correspond to the Referential Geometric Entities (RGEs), creating sets of B-curves and splines, and creating parts of the surface model using loft and blend function. These parts were further merged into complete surface model of the hip bone (Tufegdžić et al. 2013).

5.1.2 Rationale for Developing a New Method

Reconstruction of medical images in 3D today is an integral part of biomedical research. Registration of multiple cross-sections is of great importance for correct 3D visualization and morphometric analysis of structures (Angelopoulou et al. 2015). CT and MRI are often used in clinical diagnosis and surgery planning, but their use as an imaging modality in interventions is limited due to lack of space in operating rooms and requirements for real-time operating procedures (Yaoa and Taylor 2012). Typical tomodensitometry methods enable obtaining exact 3D information about the human body anatomy, but high radiation doses which are harmful to the patient, large amount of information which should be collected and processed, as well as their price make them less functional (Benameur et al. 2001; Fattah 2013). X-ray radiography is the golden standard for obtaining medical images in orthopedic diagnostics, and radiographic projections still play an important role in diagnosis, surgery, and planning therapeutic procedures (Benameur et al. 2001; Fattah 2013; Lamecker et al. 2006). Belonging to the group of diagnostic methods that is characterized by low

cost, mobility, uniform imaging speed and low doses of ionizing radiation (compared to CT), it bears no risk for patients who have ferromagnetic implants (compared to classic MRI machines). The evaluation of orthopedic trauma in traditional surgery planning is based on a small number of 2D radiographic projections in vast number of cases (Fattah 2013; Ehlke et al. 2013).

A number of open source or commercial software packages have been developed to visualize volume data and obtain 3D polygonal mesh bone models and export them to STereoLithography (STL) format, from medical CT images recorded in DICOM (Digital Imaging and Communications in Medicine) format. Some examples are 3D Slicer, 3D-DOCTOR, Amira, democratiz3D, ImageVis3D, MeVisLab, Mimics, OsiriX, etc. But, regardless of the program, the construction of a 3D polygonal hip bone model must be carried out through the following phases: data collection, image segmentation and surface generation. In cases when the volumetric images of the bones are complete and of high quality, their polygonal model will be meaningful and sophisticated. However, in a large number of cases, when due to the poor quality of the image the boundaries of the bones are insufficiently clear, it is necessary to conduct the so-called model healing. This process takes a long time and requires a lot of effort.

The first step is always collecting CT data which means that the patient must be exposed to radiation doses that are significantly higher than those during imaging by other conventional methods, such as radiography. In many cases, the patient has already been exposed to certain doses of radiation in the previous period and it is not possible to take another CT image. In addition, in case of a high degree of osteoporosis, the quality of the CT image is such that it prevents obtaining clouds of points of the entire bone volume. Sometimes, due to great trauma or bone disease, some parts of the bones no longer physically exist, so it is not possible to obtain data on that part based on the images. In such cases, reconstructing the required 3D bone model is impossible.

Therefore, it was necessary to develop a new method that enables obtaining a 3D surface model of the human hip bone, in the cases when the input data are incomplete and medical images do not contain all bone elements. This especially refers to situations when the only available data are 2D X-ray images in Anterior–Posterior (A-P) and lateral projection, which is of particular importance.

5.1.3 Reconstruction of 3D Models from 2D Images—State of Art

In order to form a 3D model for a specific patient from incomplete data obtained by ultrasound or X-ray imaging, reconstruction of surfaces is a good technology for preoperative planning or for navigation during operations (Yaoa and Taylor 2012). In recent years, methods for reconstructing a personalized bone shape from incomplete data using statistical shape modeling techniques are applied to a large extent. The

main idea for shape reconstruction based on a statistical model is to find statistically probable values of model parameters that minimize the adjustment criteria between the initial model and the available information, which is patient specific. The type of information used for reconstruction is common to all methods. The information contains data on explicit morphological characteristics, such as parts of surfaces, contours or points. These methods are mainly based on multilinear regression (Blanc et al. 2012).

Some problems may arise when reconstructing pathological deformities or missing anatomical structures, when the normal natural appearance is unknown. In a large number of cases, objective criteria for guiding the remodeling and reshaping processes are lacking, and operators are guided by subjective assessment (e.g., aesthetics) (Lamecker 2008). Another group of methods use constraints based on nonlinear functions of point positions, but only explicit landmarks can be treated (Blanc et al. 2012).

Reconstruction of 3D unknown object geometry from 2D images is a problem that needs special attention, since it is necessary to generate a model with only a few (2 or more) radiographic projections (Benameur et al. 2001; Fattah 2013; Lamecker et al. 2006). The lack of information due to the small number of images can be compensated by the inclusion of prior knowledge, formulated to represent the shape of the bones in a way that allows deformation of the model based on the entities taken from the image. Assuming that the entities taken from the image, together with the information from the previously defined form (template), provide sufficient information, the patient's anatomy could be obtained, with the required accuracy. The template model implies information that is specific to a given bone, and is actually an estimate of the initial shape, in the form of a Statistical Shape Model (SSM) (Fattah 2013).

3D shape reconstruction from a set of incomplete 2D projection images is important for a large number of medical applications. Image-guided intervention systems require a personalized 3D anatomical model, which should be connected to the intra-operating system. Some alternatives suggest 3D model generation from calibrated radiographic projections, but it is necessary to integrate previous knowledge for a successful 3D reconstruction, e.g., using a statistical model shape. In the case of incomplete data, two groups of procedures are applied for the reconstruction of the precise anatomical shape of the bones: statistical deformation model and PDM (Baka et al. 2010).

Hybrid 2D-3D deformable registration was performed by combining a landmark registration from one A-P projection of the hip one with SSM based on a 2D-3D reconstruction scheme. Landmark registration was used to find the initial scale and initial rigid transformation between A-P projection and SSM (Zheng 2009). Similarity criteria, based on surface normal and distance was used for determining landmarks in the process of 3D reconstruction (Baka et al. 2010).

The statistical model of the pelvis was made from a collection of CT images, and a simulation of X-rays (known as Digitally Reconstructed Radiographs—DRRs) from CT data for a specific patient. The model was presented in the form of a network of

tetrahedrons. These nets have great flexibility and can adapt to the anatomical shape (Yaoa and Taylor 2012).

5.2 Parameter-Based Patient Specific 3D Model

Due to the fact that CT became the golden standard for generating 3D geometrical bone models with the high accuracy, we used a sample of 38 male CT scans of the right hip bone, obtained with Toshiba MSCT scanner Aquillion 64 (120 kV, 150 mA, thickness 1 mm, in-plane resolution 0.781 × 0.781 mm (pixel size), acquisition matrix 512 × 512, field of view (FOV) 400 × 400 mm). The bones affected by pathological changes, fractures and deformities are excluded from the sample, so it has been reduced to 32 healthy bones, aged from 20 to 83 years (average 64 years).

Data from CT scans, written in DICOM format are converted to STL format and exported to CAD program with the aim to obtain polygonal models of bones. For some models it was necessary to reconstruct and heal the surfaces, eliminate errors and smooth sharp edges.

Research is conducted through a few steps, similar to those presented in Trajanovic et al. (2018) and Tufegdzic et al. (2015):

- Processing CT scans and generating 3D models from DICOM images
- Model reconstruction in CAD program and obtaining polygonal models
- Determining landmarks and parameters
- Measuring parameter values
- Statistical analysis of data and calculating statistical values
- Determining the correlations between parameters
- Choosing, testing and establishing proper regression models for parameters, and selecting of the proper regression model, according to statistical indicators such as the level of statistical significance and the highest value of variance.

At each polygonal model of the human hip bone, a sufficient number of anatomical points in the form of bilateral landmarks is separated in order to capture the shape of all constitutive bones. These 34 bilateral landmarks, presented on the right and left ilium, ischium and pubic bones, are easily identified and recognized on radiographic projections.

Bilateral landmarks defined and separated at the wing of ilium bone are (Trajanovic et al. 2018; Tufegdzic et al. 2015):

1. The most superior point on the iliac crest
2. The most lateral iliac crest point
3. Anterior superior iliac spine (ASIS)
4. Anterior inferior iliac spine (AIIS)
5. Posterior superior iliac spine (PSIS)
6. Posterior inferior iliac spine (PIIS)
7. The most superior point at the acetabular limbus

8. The deepest point at greater sciatic notch
9. The superior point at the sacroiliac joint
10. The inferior point at the sacroiliac joint.

ZS—the point of intersection between the posterior gluteal line with the outer lip of the iliac crest.
DS—the point of intersection between the inferior gluteal line with anterior edge of the iliac crest.
PS—the point of intersection between the anterior gluteal line with anterior end of the iliac crest (at the superior edge of the hip bone).
NISUA—the deepest point at the anterior iliac notch at the anterior edge.
NISUP—the deepest point at the anterior iliac notch at the posterior edge.

At the ischium and pubic bone the following bilateral landmarks are defined and separated:

11. The deepest point in acetabular fossa (Ruiz 2005; Lubovsky et al. 2010)
12. Point at the acetabular rim where ilium and ischium bone are connected (Betti et al. 2013; Ruiz 2005; Lubovsky et al. 2010)
13. Point at the acetabular rim where ilium and superior pubis ramus are connected (Betti et al. 2013; Ruiz 2005; Lubovsky et al. 2010)
14. The most inferior point of the posterior end of the lunate surface of the acetabulum (Betti et al. 2013; Lubovsky et al. 2010)
15. The tip of the ischium spine (Betti et al. 2013; Decker 2010; Margam et al. 2013; O'Connell 2004)
16. The deepest point at the lesser sciatic notch
17. The most prominent point at the upper part of the ischial tuberosity (Betti et al. 2013; Ruiz 2005; Margam et al. 2013; O'Connell 2004)
18. The most lateral point at the posterior edge of the ischial tuberosity (Betti et al. 2013; Ruiz 2005)
19. The tip of the ischial tuberosity, the most prominent point at the anterior edge of the ischial tuberosity (Betti et al. 2013)
20. The most inferior point at the ischial tuberosity (Betti et al. 2013)
21. The most posterior point of the obturator foramen (Betti et al. 2013; Ruiz 2005; O'Connell 2004)
22. The most anterior point of the obturator foramen (Ruiz 2005; O'Connell 2004)
23. The lowest point at the ischiopubic ramus (Ruiz 2005; Decker 2010; O'Connell 2004; Dhindsa et al. 2013)
24. The most superior point of the obturator foramen (Betti et al. 2013; Ruiz 2005; O'Connell 2004)
25. The most inferior point where inferior pubis ramus and ischium ramus are connected (Ruiz 2005; O'Connell 2004)
26. The most inferior point of the anterior end of the lunate surface of the acetabulum (Betti et al. 2013)
27. Pubic tubercle, as the most anterior point at the pubic tubercle (Betti et al. 2013; Lubovsky et al. 2010; Decker 2010)

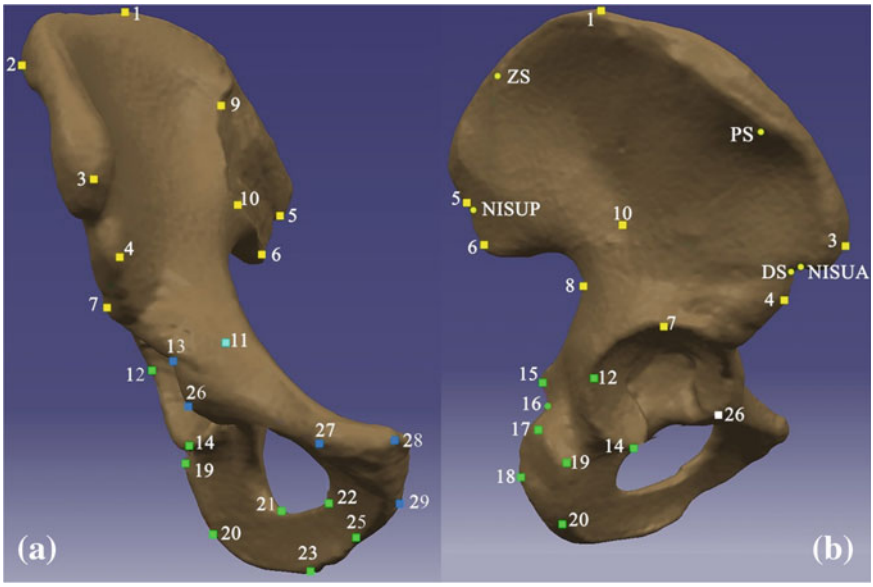

Fig. 5.1 Bilateral landmarks at the ilium, ischium and pubic bone **a** A-P projection, **b** lateral projection

28. The most superior point on the superior edge of the medial aspect of the pubic symphysis (Betti et al. 2013; Ruiz 2005; O'Connell 2004)
29. The most inferior point on the inferior edge of the medial aspect of the pubic symphysis (Betti et al. 2013; Ruiz 2005; O'Connell 2004).

Bilateral landmarks in A-P and lateral projection at the ilium, ischium and pubic bone are presented in Fig. 5.1.

Anatomical landmarks on ilium, ischium and pubic bone are interconnected by straight lines. These lines, defined by linear distance between chosen anatomical landmarks, represent parameters. From the points listed above, it is possible to create 105 parameters at the wing of ilium bone, and 406 parameters at the ischium and pubic bone. In our research we have used 58 parameters at the hip bone, because that number of parameters is sufficient to fully morphologically define the complex form of the human ilium, ischium and pubic bones. For better preview, the parameters will be listed depending on which bone they belong (26 at the ilium bone, 19 at the ischium bone, and 13 at the pubic bone). This will also make it easier for their practical implementation. Parameters at the ilium bone are presented and described in Table 5.1.

Selected parameters of the human ilium bone are presented in Fig. 5.2.

At the ischium bone, 18 parameters are separated. One additional parameter is also separated, labeled as d_{27} and considered common for ilium and ischium bone due to the fact that it connects landmark 8 (as the deepest point at greater sciatic notch) and landmark 12 from different bones. At the pubic bone 10 parameters are separated,

Table 5.1 Parameters at the wing of ilium bone (Trajanovic et al. 2018)

No.	Parameter	Label	Points
1	Distance between anterior and posterior superior iliac spines	d_1	3–5
2	Distance between anterior and posterior inferior iliac spines	d_2	4–6
3	Distance between anterior superior and posterior inferior iliac spines	d_3	3–6
4	Distance between the most lateral iliac crest point and the superior point at the sacroiliac joint	d_4	2–9
5	Distance between the point of intersection between the inferior gluteal line with anterior edge of the iliac crest and the inferior point at the sacroiliac joint	d_5	DS–10
6	Distance between the deepest points at anterior–posterior iliac notches	d_6	NISUA–NISUP
7	Distance between the point of intersection between the anterior gluteal line with anterior end of the iliac crest and the point of intersection between the posterior gluteal line with the outer lip of the iliac crest	d_7	PS–ZS
8	Distance between anterior inferior iliac spine and the deepest point at greater sciatic notch	d_8	4–8
9	Distance between the most superior point on the iliac crest and the deepest point at greater sciatic notch	d_9	1–8
10	Distance between the posterior inferior iliac spine and the point of intersection between the posterior gluteal line with the outer lip of the iliac crest	d_{10}	6–ZS
11	Distance between the most superior point on the iliac crest and the most superior point at the acetabular limbus	d_{11}	1–7
12	Distance between posterior inferior iliac spine and the deepest point at the iliac notch at the posterior edge	d_{12}	6–NISUP
13	Distance between the most lateral iliac crest point and anterior superior iliac spine	d_{13}	2–3
14	Distance between posterior superior iliac spine and the point of intersection between the posterior gluteal line with the outer lip of the iliac crest	d_{14}	5–ZS
15	Distance between the most superior point on the iliac crest and posterior superior iliac spine	d_{15}	1–5
16	Distance between the most superior point on the iliac crest and anterior superior iliac spine	d_{16}	1–3
17	Distance between the most superior point on the iliac crest and posterior inferior iliac spine	d_{17}	1–6
18	Distance between the most superior point on the iliac crest and posterior inferior iliac spine	d_{18}	1–4
19	Distance between the most superior point on the iliac crest and the point of intersection between the posterior gluteal line with the outer lip of the iliac crest	d_{19}	1–ZS

(continued)

Table 5.1 (continued)

No.	Parameter	Label	Points
20	Distance between the most superior point on the iliac crest and the most lateral iliac crest point	d_{20}	1–2
21	Distance between anterior superior iliac spine and the deepest point at the anterior iliac notch at the anterior edge	d_{21}	3–NISUA
22	Distance between the superior and the inferior point at the sacroiliac joint	d_{22}	9–10
23	Distance between anterior inferior iliac spine and the deepest point on the anterior iliac incisures at the anterior edge	d_{23}	4–NISUA
24	Distance between posterior superior iliac spine and the deepest point on the posterior iliac notch at the posterior edge	d_{24}	5–NISUP
25	Distance between the most superior point at the acetabular limbus and the deepest point at greater sciatic notch	d_{25}	7–8
26	Distance between the most superior point at acetabular limbus and anterior inferior iliac spine	d_{26}	7–4

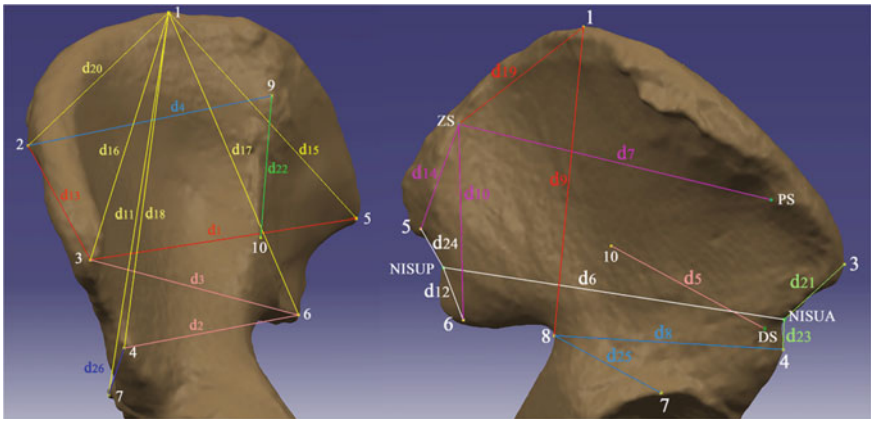

Fig. 5.2 Parameters at the ilium bone. Modified from Trajanovic et al. (2018)

as well as 3 additional parameters (d_{53}, d_{57} and d_{58}) that connect landmarks from different bones (26–14, 11–4 and 13–4, respectively). These parameters are presented and described in Table 5.2.

Selected bilateral landmarks and parameters are presented in Fig. 5.3 in A-P and lateral projection of the human ischium and pubic bone. Parameters at the ischium bone are displayed with cyan lines and parameters at the pubic bone with yellow lines. Parameters belonging to different bones appear as dash-dot lines (blue, green and white).

At each of the constitutive bones, parameters are divided into 2 groups. Parameters which can be easily measured in A-P and lateral projections of the hip bone are

Table 5.2 Parameters at the ischium and pubic bone

No.	Parameter	Label	Points
1	Distance between the point of maximum curvature (the deepest point) at greater sciatic notch and the point at the acetabular rim where ilium and ischium bone are connected	d_{27}	8–12
2	Distance between the tip of the ischium spine and the point at the acetabular rim where ilium and ischium bone are connected	d_{28}	15–12
3	Distance between the tip of the ischium spine and the deepest point at the lesser sciatic notch	d_{29}	15–16
4	Distance between the deepest point at the lesser sciatic notch and the point at the acetabular rim where ilium and ischium bone meet	d_{30}	16–12
5	Distance between the most prominent point at the upper part of the ischial tuberosity and the point at the acetabular rim where ilium and ischium bone are connected	d_{31}	17–12
6	Distance between the most lateral point at the posterior edge of the ischial tuberosity and the point at the acetabular rim where ilium and ischium bone are connected	d_{32}	18–12
7	Distance between the most prominent point at the upper part of the ischial tuberosity and the most lateral point at the posterior edge of the ischial tuberosity	d_{33}	17–18
8	Distance between the most lateral point at the posterior edge of the ischial tuberosity and the most prominent point at the anterior edge of the ischial tuberosity	d_{34}	18–19
9	Distance between the most lateral point at the posterior edge of the ischial tuberosity and the most inferior point at the ischial tuberosity	d_{35}	18–20
10	Distance between the most prominent point at the anterior edge of the ischial tuberosity and the point at the acetabular rim where ilium and ischium bone are connected	d_{36}	19–12
11	Distance between the most prominent point at the anterior edge of the ischial tuberosity and the most inferior point of the posterior end of the lunate surface of the acetabulum	d_{37}	19–14
12	Distance between the most prominent point at the anterior edge of the ischial tuberosity and the most inferior point at the ischial tuberosity	d_{38}	19–20
13	Distance between the most inferior point of the posterior end of the lunate surface of the acetabulum and the most inferior point at the ischial tuberosity	d_{39}	14–20
14	Distance between the most inferior point at the ischial tuberosity and the most posterior point of the obturator foramen	d_{40}	20–21
15	Distance between the most inferior point at the ischial tuberosity and the lowest point at the ischiopubic ramus	d_{41}	20–23
16	Distance between the most posterior point of the obturator foramen and the lowest point at the ischiopubic ramus	d_{42}	21–23
17	Distance between the most anterior point of the obturator foramen and the lowest point at the ischiopubic ramus	d_{43}	22–23

(continued)

Table 5.2 (continued)

No.	Parameter	Label	Points
18	Distance between the lowest point at the ischiopubic ramus and the most inferior point where inferior pubis ramus and ischium ramus are connected	d_{44}	23–25
19	Distance between the most anterior point of the obturator foramen and the most inferior point where inferior pubis ramus and ischium ramus are connected (O'Connell 2004)	d_{45}	22–25
20	Distance between the most inferior point where inferior pubic ramus and ischium ramus are connected and the most inferior point on the inferior edge of the medial aspect of the pubic symphysis (O'Connell 2004)	d_{46}	25–29
21	Distance between the most anterior point of the obturator foramen and the most inferior point on the inferior edge of the medial aspect of the pubic symphysis (Gupta et al. 2014)	d_{47}	22–29
22	Distance between the most superior point on the superior edge of the medial aspect of the pubic symphysis and the most inferior point on the inferior edge of the medial aspect of the pubic symphysis (Betti et al. 2013; Decker 2010; O'Connell 2004; Boulay et al. 2006)	d_{48}	28–29
23	Distance between the most anterior point of the obturator foramen and the most superior point on the superior edge of the medial aspect of the pubic symphysis	d_{49}	22–28
24	Distance between pubic tubercle and the most superior point on the superior edge of the medial aspect of the pubic symphysis (Betti et al. 2013)	d_{50}	27–28
25	Distance between pubic tubercle the most anterior point of the obturator foramen	d_{51}	27–22
26	Distance between pubic tubercle and most inferior point of the anterior end of the lunate surface of the acetabulum	d_{52}	27–26
27	Distance between most inferior point of the anterior end of the lunate surface of the acetabulum and the most inferior point of the posterior end of the lunate surface of the acetabulum	d_{53}	26–14
28	Distance between pubic tubercle and the point at the acetabular rim where ilium and superior pubis ramus meet (Sharma and Vijayvergiya 2013)	d_{54}	27–13
29	Distance between pubic tubercle and the deepest point in acetabular fossa (O'Connell 2004; Okoseimiema and Udoaka 2013)	d_{55}	27–11
30	Distance between the point at the acetabular rim where ilium and superior pubis ramus are connected and the deepest point in acetabular fossa	d_{56}	13–11
31	Distance between the deepest point in acetabular fossa and anterior inferior iliac spine (Boulay et al. 2006)	d_{57}	11–4
32	Distance between the point at the acetabular rim where ilium and superior pubis ramus are connected and the deepest point in acetabular fossa	d_{58}	13–4

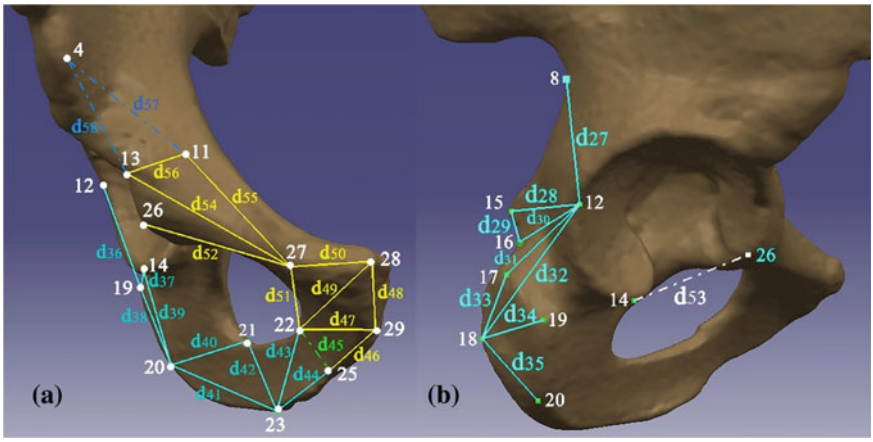

Fig. 5.3 Selected parameters at the ischium and pubic bone **a** A-P projection, **b** lateral projection

treated as independent variables and classified in the first group. The second group of parameters includes dependent variables, with the possibility to set up regression equations (Trajanovic et al. 2018).

Independent variables are:

1. At the ilium bone: d_1, d_2, d_3, d_4, d_8, d_9, d_{15}, d_{16}, d_{17} and d_{22} (10 parameters) (Trajanovic et al. 2018)
2. At the ischium bone: d_{27}, d_{32}, d_{38}, d_{40}, d_{41}, d_{42} and d_{45} (7 parameters)
3. At the pubic bone: d_{47}, d_{48}, d_{49} and d_{57} (4 parameters).

Dependent variables are:

1. At the ilium bone: d_5, d_6, d_7, d_{10}, d_{11}, d_{12}, d_{13}, d_{14}, d_{18}, d_{19}, d_{20}, d_{21}, d_{23}, d_{24}, d_{25} and d_{26} (16 parameters) (Trajanovic et al. 2018)
2. At the ischium bone: d_{28}, d_{29}, d_{30}, d_{31}, d_{33}, d_{34}, d_{35}, d_{36}, d_{37}, d_{39}, d_{43} and d_{44} (12 parameters)
3. At the pubic bone: d_{46}, d_{50}, d_{51}, d_{52}, d_{53}, d_{54}, d_{55}, d_{56} and d_{58} (9 parameters).

All parameters' values are measured over the whole sample and values for descriptive statistics are calculated. Correlation coefficients between parameters from independent and dependent groups are calculated with the aim to determine dependencies between variables. For each of the parameters from the second group, choosing regression models for testing was done by using scatter plots. Linear ($d_j = a + b \cdot d_i$), squared ($d_j = a \cdot d_i^2, d_j = a + b \cdot d_i^2, d_j = a + b \cdot d_i + c \cdot d_i^2$), third-degree polynomial ($d_j = a + b \cdot d_i + c \cdot d_i^2 + d \cdot d_i^3$), logarithmic ($d_j = a \cdot \ln(d_i)$, $d_j = a + b \cdot \ln(d_i)$), and exponential ($d_j = a \cdot e^{b \cdot d_i}$) models proved to be the best fitted models. Regression coefficients a, b, c and d in regression equation are calculated using least square method, while d_j stands for dependent variable, and d_i stands for independent variable.

The basic condition for the acceptance of the model is established in such way that the value of statistical significance (p-value) must be less than 0.01 for all parameters a, b, c and d. Value of variance R^2 is also determined. From all the models which satisfy the set condition, the one with the highest R^2 is selected according to methodology described in Trajanovic et al. (2018) and Tufegdzic et al. (2015).

Adopted regression models for ilium, ischium and pubic bone, so as the values for R^2 are presented in Table 5.3.

An exception was made when determining the regression model for the parameter d_{25}, where the correlation coefficient had a higher value for the parameter d_{11}, in relation to the correlation coefficient for the parameter d_2. The values of R^2 are significantly higher in the case of dependence between the parameters d_{25} and d_{11} than in the case of dependence from d_{25} on d_2. However, due to the fact that the value of the parameter d_{11} is obtained from the regression equation, which would increase the computational error, a model in which the parameter d_{25} is calculated as a function of d_2 has been adopted.

Various models presented in Table 5.3 may be associated with the complex shape of the human hip bone. Only non-linear regression is suitable for describing the proper dependencies between the parameters at the bones, such as 11 quadratic, 13 exponential, and 13 logarithmic. For example, at the ilium bone 3 quadratics, 8 exponential and 5 logarithmic, at the ischium bone 6 quadratics, 3 logarithmic and 3 exponential, and at the pubic bone 2 quadratic, 5 logarithmic and 2 exponential models, are adopted.

On the other hand, all regression models can be considered statistically significant based on the values of variance R^2. The only exception is the parameter d_{21}, since it is difficult to choose the appropriate model because the level of statistical significance for all tested models is greater than 0.01. However, there are few regression models for discussion according to the values of variance R^2. Some examples are d_{10}, d_{12} and d_{14} at the ilium bone, d_{33} and d_{37} at the ischium bone, so as d_{50} at the pubic bone (Table 5.3). Some improvements should be made by increasing the number of bones in the sample. Additional issues to be taken into consideration are the regression models for the parameter d_{35} at the ischium bone and the parameter d_{53} at the pubic bone because their values of variance R^2 are significantly smaller compared to the other value.

There are some interesting conclusions to be drawn, such as dependencies for parameters at the ischium and pubic bone. Parameters like d_{28} and d_{33} at the ischium bone are dependent from parameters d_8 and d_{17}, at the ilium bone respectively, while parameters at the pubic bone d_{54} and d_{55} show dependencies from parameters d_2 and d_1 respectively, also at the ilium bone.

In order to test the obtained and adopted models, all parameters from both groups are measured at one randomly chosen right male hip bone. Predicted values for dependent values are calculated, according to regression equations from Table 5.3. The differences between the measured and prediction values were calculated and presented in the form of absolute errors. For the purpose of additional comparison, considering the fact that the range of values of the measured parameters is large—from 11.185 to 126.074 mm at the ilium bone, from 11.488 to 87.543 mm at the

Table 5.3 Regression models for the parameters at the ilium, ischium and pubic bone. Expanded from Tufegdzic et al. (2015)

No.	Parameter	Adopted model	R^2
1	d_5	$d_5 = 45.99044 + 0.00510 \cdot d_8^2$	0.5179
2	d_6	$d_6 = 48.68143 \cdot e^{0.00623 \cdot d_1}$	0.6679
3	d_7	$d_7 = 41.51965 \cdot e^{0.00974 \cdot d_9}$	0.4326
4	d_{10}	$d_{10} = 39.82035 + 0.00249 \cdot d_{17}^2$	0.1739
5	d_{11}	$d_{11} = -236.556 + 77.831 \cdot \ln(d_9)$	0.4889
6	d_{12}	$d_{12} = 0.001189 \cdot d_{17}^2$	0.0956
7	d_{13}	$d_{13} = 9.1589 \cdot e^{0.015011 \cdot d_{16}}$	0.4364
8	d_{14}	$d_{14} = 10.47298 \cdot \ln(d_{15})$	0.0451
9	d_{18}	$d_{18} = 89.80292 \cdot e^{0.00312 \cdot d_2}$	0.2707
10	d_{19}	$d_{19} = -523.964 + 124.585 \cdot \ln(d_9)$	0.3477
11	d_{20}	$d_{20} = 38.09926 \cdot e^{0.00754 \cdot d_4}$	0.3467
12	d_{21}	$d_{21} = 64.25015 \cdot e^{-0.00746 \cdot d_{16}}$	0.1185
13	d_{23}	$d_{23} = 4.985783 \cdot \ln(d_{16})$	0
14	d_{24}	$d_{24} = 3.758796 \cdot \ln(d_{17})$	0
15	d_{25}	$d_{25} = 33.12012 \cdot e^{0.00408 \cdot d_2}$	0.2198
16	d_{26}	$d_{26} = 2.52512 \cdot e^{0.01479 \cdot d_8}$	0.5049
17	d_{28}	$d_{28} = 30.49856 + 0.00316 \cdot d_8^2$	0.4510
18	d_{29}	$d_{29} = 13.22304 + 0.00355 \cdot d_{42}^2$	0.2205
19	d_{30}	$d_{30} = 27.09725 + 0.00442 \cdot d_{32}^2$	0.4281
20	d_{31}	$d_{31} = 7.107463 \cdot e^{0.026285 \cdot d_{32}}$	0.7269
21	d_{33}	$d_{33} = 6.843322 \cdot \ln(d_{17})$	0
22	d_{34}	$d_{34} = 2.49362 + 0.00876 \cdot d_{38}^2$	0.4147
23	d_{35}	$d_{35} = 6.083382 \cdot \ln(d_{42})$	0.1468
24	d_{36}	$d_{36} = 13.27352 + 0.00713 \cdot d_{32}^2$	0.5765
25	d_{37}	$d_{37} = 72.4284 - 12.0838 \cdot \ln(d_{38})$	0.1972
26	d_{39}	$d_{39} = 29.69258 \cdot e^{0.01535 \cdot d_{32}}$	0.2034
27	d_{43}	$d_{43} = 109.3173 - 2.3663 \cdot d_{41} + 0.00161 \cdot d_{41}^2$	0.6699
28	d_{44}	$d_{44} = 126.0179 \cdot e^{-0.0254 \cdot d_{41}}$	0.6537
29	d_{46}	$d_{46} = -46.4303 + 18.9263 \cdot \ln(d_{47})$	0.5187
30	d_{50}	$d_{50} = 6.955778 \cdot \ln(d_{42})$	0.1252
31	d_{51}	$d_{51} = -98.9599 + 37.3463 \cdot \ln(d_{49})$	0.4869
32	d_{52}	$d_{52} = 34.32717 \cdot e^{0.00905 \cdot d_{49}}$	0.2256
33	$d_{53}{}^*$	$d_{53} = 7.368643 \cdot \ln(d_{57})$	0.1097
34	d_{54}	$d_{54} = -142.760 + 43.089 \cdot \ln(d_2)$	0.3809
35	d_{55}	$d_{55} = 36.4147 \cdot e^{0.00436 \cdot d_1}$	0.3079
36	d_{56}	$d_{56} = 24.10751 + 0.00281 \cdot d_{57}^2$	0.3626

(continued)

Table 5.3 (continued)

No.	Parameter	Adopted model	R^2
37	d_{58}	$d_{58} = 14.90829 + 0.00560 \cdot d_{57}^2$	0.5134

*A logarithmic model was adopted for parameter d_{53}, although the value of R^2 (0.466) for the third-degree polynomial model is significantly higher, due the fact that the calculated parameter value had showed a significantly higher absolute error value compared to the adopted model, as well as to simplify calculation

Table 5.4 Average values of absolute and relative errors for the ilium, ischium, pubic and hip bone

	Bone			
	Ilium	Ischium	Pubic	Hip
Average values of absolute error (mm)	2.881	2.309	1.291	2.161
Average values of relative error (mm)	0.058	0.088	0.042	0.062

ischium bone, and 10.584 to 87.331 mm at the pubic bone, the values of relative errors were also calculated.

The values for errors, especially relative errors, could be considered in correlation with some statistical indicators, such as minimum and maximum values for measured parameters, values for variation and in particular, values for standard deviation over the sample. Increasing the number of samples will lead to further improvements.

For the purpose of comparative analysis of the obtained results, the average values of absolute and relative errors are calculated for the entities from which the hip bone is constituted as well as for the complete bone. The results are shown in Table 5.4.

The average value of the absolute error between the predictive and measured values of the parameters is the highest for the ilium, and the lowest for the pubic bone. This is understandable because the average values of the measured parameters are the smallest for the pubic bone. The average relative error is the largest for the ischium and the smallest for the pubic bone, while the average value of the relative error for the complete bone is in fact closest to the average value of the relative error for the ilium bone, which is the most complex geometric entity on the human hip bone.

5.3 Method of Parametric Regions

The process of geometric reconstruction during which polygonal models of human hip bones are formed from point clouds, included in the sample, represents the initial phase in the Method of parametric regions. After healing and smoothing, anatomical landmarks were determined on each of the polygonal models. Parameters were defined as linear distances between the landmarks. After establishing correlations

between the measured parameter values, appropriate regression models were tested and selected using tools for mathematical (statistical) modeling.

In order to unambiguously determine the position of anatomical landmarks and all points on the surface of the bones whose coordinates need to be measured, an anatomical coordinate system of the pelvic bone was formed on the basis of anatomical landmarks. The Method of Anatomical Features (described in Chap. 2) applied in this phase of research has been extended and adapted to the complex hip bone anatomy needs, in Geometric morphometry process.

Cutting polygonal models with planes determined by the given parameters, using Quick Plane definition function in CATIA Shape module, results in the set of 26 intersection curves. Another set of intersection curves is obtained by cutting the polygonal models with planes at equal distances of 4 mm. These planes are perpendicular to the given parameters. The intersections of these two sets of curves represent points, whose values of coordinates (X, Y and Z) are measured in right-handed orientation anatomical coordinate system of the hip bone (Trajanovic et al. 2018). These values are taken as the input values for the statistical program. After establishing correlations between coordinates' and parameters' values, different linear and nonlinear regression models (quadratic, logarithmic and exponential) are tested for 1195 intersection points. Proper regression models are established using the criteria for the level of statistical significance ($p < 0.01$) and the highest value for the coefficient of determination (R^2) described in Trajanovic et al. (2018).

Based on the obtained results some conclusions should be drawn. The largest number of obtained regression models is nonlinear, for X coordinate is 98.83%, for Y coordinate is 99.58%, and for Z coordinate is 96.47%, from overall number of equations. The number of linear models is for X coordinate 1.14% and for Y coordinate 0.42%. These values should be considered as statistical errors, and logarithmic models should be chosen as proper regression models. In the group of nonlinear models, the most common ones are logarithmic models, especially at the Z coordinate (93.00%). The greatest variability is shown for X coordinate, given the fact that the positions of the points, e.g., the values of these coordinates, follow the complex geometry of the hip bone to a great extent.

For polygonal model parts that correspond to the edges of the hip bone (the superior edge and the parts of the anterior and posterior edge), the points are defined in such manner that the surfaces which correspond to the edges are fully described. The superior edge of the hip bone which extends from point 3 (ASIS) to point 5 (PSIS) is described by the parts of the polygonal model above the parameters d_{13}, d_{20}, d_{19} and d_{14}. At curves obtained by intersecting the polygonal model with the planes perpendicular to the aforementioned parameters, additional points are defined at distances of 5 mm from the intersection points on the curves through the given parameters at both sides of the hip bone (outer and inner). The part of the anterior edge of the hip bones that extends between anterior iliac spines (points 3 and 4) is described by parts of the polygonal model below the parameter d_{21} and right from the parameter d_{23}. Additional points were obtained in the same way as with the superior edge, at the curves that are perpendicular to the parameters d_{21} and d_{23}.

The part of the posterior edge of the hip bone between posterior iliac spines (points 5 and 6) was described by the parts of polygonal model left from the parameters d_{24} and d_{12}. For describing the part of the edge which extends from PIIS (point 6) to the deepest point at greater sciatic notch (point 8), one more measure is introduced. In order to describe the geometry of this part of the posterior edge, it is necessary to measure the distance between point 6 and the point obtained at the intersection of parameters d_3 and d_9 in the plane projection. Based on this distance it is possible to calculate the required number of intersection curves using the expression for the number of curves N_c presented in Trajanovic et al. (2018), where mean value of the measured distance d_{3x} is used as the average value of the parameters d_{sr}.

After measuring the values of the coordinates of all selected points on the edges of the hip bone, the methodology used for choosing proper regression models for points at the curves through the parameters was applied. The corresponding mathematical models for the point's coordinates in function of the respective parameter are obtained. The number of points on the curves was chosen so that a particular point covers the coordinate values in at least one half of the sample ($N \geq 16$).

For describing the geometry of the edges, e.g., the parts of the edges at the wing of ilium bones, it was necessary to define a total of 454 points. Linear dependences for the point's coordinates of on the values of parameters cannot describe the geometry on these parts of the hip bone. At the parts of the anterior and posterior edge all regression models for X coordinate are logarithmic, as well as for the Z coordinate at the posterior part of the edge. Variability in regression models is the greatest for the X coordinate at the superior edge of the hip bone bone (82.96% is logarithmic, 15.82% is square), for Y coordinates at the part of the posterior edge (31.52% is square and logarithmic, while 36.96% is exponential), and for Z coordinates at the part of the anterior edge (40.74% is logarithmic, 51.85% is exponential). The variability for the Y coordinates at the part of the posterior edge results from geometric shapes that appear on the part of the edge below the parameter d_3.

The predictive values of the X, Y and Z coordinates of all these points were calculated in the first iteration, and a polygonal model of the wing of ilium bone was constructed. Some additional operations like optimization, smoothing and increasing the neighbor value lead to improving the model, but the surface 3D model's geometry was disturbed. Bearing in mind that the obtained model has a certain number of holes that have to be filled in the areas between neighboring parameters, some additional points were defined. After thorough analysis, ten parametric regions were defined. Parametric regions are actually the areas between two neighboring parameters. At the wing of ilium bone, ten parametric regions were separated: parametric region d_{14}–d_{15}, parametric region d_{15}–d_{19}, parametric region d_{17}–d_{15}, parametric region d_{17}–d_9, parametric region d_9–d_{11}, parametric region d_{11}–d_{18}, parametric region d_{18}–d_{16}, parametric region d_{16}–d_{20}, parametric region d_{16}–d_{13} and parametric region d_8–d_{25}–d_{26}. Labels for parametric regions were assigned according to parameters that represent boundaries for the given region (Trajanovic et al. 2018). Parametric regions and the parts of the edges (colored in yellow) at the wing of ilium bone are presented in Fig. 5.4.

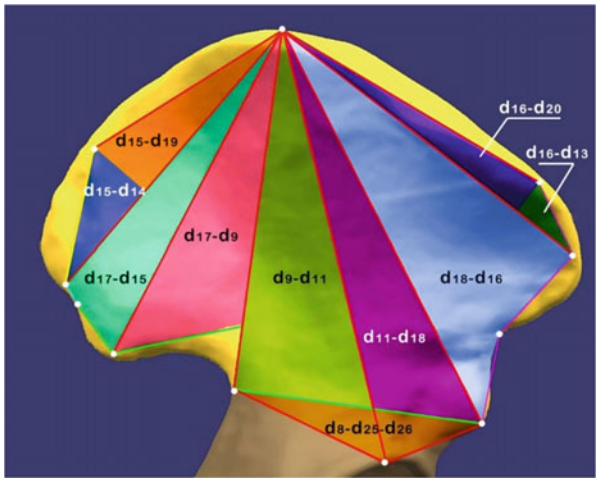

Fig. 5.4 Parametric regions at the wing of ilium bone

In each parametric region, additional points on the curves perpendicular to the corresponding parameters were defined. Points were defined at equal distances of 5 mm, starting from the intersection points, at curves obtained by cutting the polygonal model with planes determined by 26 parameters, at the outer and inner side of the bone surface.

To determine additional points in parametric regions the following curves were used:

1. For parametric region d_{15}–d_{14}—curves that are perpendicular to d_{14}
2. For parametric region d_{15}–d_{19}—curves that are perpendicular to d_{19}
3. For parametric region d_{17}–d_{15}—curves that are perpendicular to d_{15}
4. For parametric region d_{17}–d_{9}—curves that are perpendicular to d_{9}
5. For parametric region d_{9}–d_{11}—curves that are perpendicular to d_{11}
6. For parametric region d_{11}–d_{18}—curves that are perpendicular to d_{18}
7. For parametric region d_{18}–d_{16}—curves that are perpendicular to d_{16}
8. For parametric region d_{16}–d_{20}—curves that are perpendicular to d_{20}
9. For parametric region d_{16}–d_{13}—curves that are perpendicular to d_{13}
10. For parametric region d_{8}–d_{25}–d_{26}—curves that are perpendicular to d_{8}.

Coordinate values regression models of points were obtained using the same methodology as in the cases of points at intersection curves at parameters and points which belong to parts of the surface that correspond to the edges. In order to obtain a regression model for any of the points in the regions, it was necessary to measure the coordinates of the given point in at least one half of the sample ($N \geq 16$). The number of additional points depends of the total surface of the region. The number of selected points is directly related to the size of the parametric region, which is limited by the given parameters, e.g., the area of the bone surface that is covered by the given region. For example, for the region d_{11}–d_{18}, number of points was 269,

while in the region d_{16}–d_{13} was only 15 points. The total number of points was 1310, after eliminating the points whose statistically significant results could not be obtained due to insufficient data. Thus, 3930 regression equations for the point's coordinates X, Y and Z in parametric regions were obtained. All obtained equations are logarithmic, because it was the only possible model with statistically significant results which satisfy the set criteria ($p < 0.01$).

Analyzing results on the number of obtained regression models leads to several conclusions. For building 3D surface model of the wing of the ilium bone it was necessary to choose 8869 regression equations for 2959 point's coordinates X, Y and Z, mostly logarithmic (7693) (Trajanovic et al. 2018). This fact could be explained by the complex surface to be created, with convex gluteal surface at the outer side, and concave iliac fossa and sacropelvic surface at the inner side. Additionally, gluteal surface, which extends from iliac crest to acetabular rim, is divided by gluteal lines to three unequal surfaces, while iliac crest which represents the superior edge is concave in front, rounding inward, and convex in back, rounding outward. These are the main reasons for small number of linear dependences for all coordinates (only 61).

The calculated predictive values of the coordinates for all points for one arbitrarily selected hip bone were used to construct the polygonal model with better quality in the second iteration. In need to manipulate a large amount of data, the implementation of equations for predicting the values of point coordinates at the surface of the wing of ilium and linking to the CAD program was automated. Therefore, during the research, three VBA (Visual Basic for Applications) short macro programs were developed: for entering the measured values of parameters and correction factors depending on the size of the X-ray, for selecting the range of points and for selecting a group of points from outer or from inner side of the bone to be exported to the CAD program. Separate sheets in Excel file for each of the predicted parameters is provided, so as for the each of the parametric regions.

Verification, done through comparative deviation and distance analysis between the initial and obtained polygonal models, confirmed significant improvement of the model. Although the method is developed for the right hip bone, it can be applied on the left ilium bone as well (Trajanovic et al. 2018).

5.3.1 Creating 3D Surface Model by Combining Parametric Regions

The method of parametric regions is flexible, because individual regions can be combined (enlarged), or divided into smaller regions, called sub-regions, depending on the needs and parts of the polygonal model of the wing of ilium bone that need to be constructed. By constructing all regions, it is possible to obtain a complete polygonal model of the wing of ilium bone.

For this purpose, individual parametric regions are aggregated with each other, and the result is then aggregated with parts of the edges, so that their polygonal models are constructed. This procedure was preceded by calculating the coordinate's predictive values for the intersection points on the curves through the parameters, the points on the selected parts of the edges of the hip bone and the points in the selected parametric regions. The selected values were exported to a CAD program and converted into point clouds, from which polygonal models were constructed.

For example, the following individual polygonal models were obtained (shown in Fig. 5.5a, where the red dots show the boundaries of the resulting polygonal models corresponding to the curves through parameters):

1. Polygonal model d_{14}–$d_{1\,5}$–$d_{19} + Ed_{14} + Ed_{19}$—created by merging the regions d_{15}–d_{14} and d_{15}–d_{19} with the parts which represent the edge above curves through parameters d_{14} and d_{19}
2. Polygonal model d_{17}–$d_{15} + Ed_{24} + Ed_{12}$—created by merging the regions d_{17}–d_{15} with the parts which represent the part of the posterior edge left from d_{24} and left from d_{12}
3. Polygonal model d_{17}–$d_9 + Ed_3$—created by merging the regions d_{17}–d_9 with part of the posterior edge below d_3
4. Polygonal model d_9–d_{11}–d_{25}—created by merging the regions d_9–d_{11} with part of the parametric region d_8–d_{25}–d_{26} (part above d_{25})
5. Polygonal model d_{11}–d_{18}–d_{26}—created by merging the regions d_9–d_{11} with part of the parametric region d_8–d_{25}–d_{26} (part above d_{26})
6. Polygonal model d_{18}–$d_{16} + Ed_{23} + Ed_{21}$—created by merging the regions d_{18}–d_{16} with parts of the anterior edge right from d_{23} and below d_{21}
7. Polygonal model d_{16}–d_{20}–$d_{13} + Ed_{20} + Ed_{13}$—created by merging the regions d_{16}–d_{20} and d_{16}–d_{13} with parts of the anterior edge above d_{20} and above d_{13}.

A similar methodology for aggregating was applied on the inner side of the wing of ilium bone, except for the regions that are near the edges. Instead of polygonal model d_{14}–d_{15}–$d_{19} + Ed_{14} + Ed_{19}$, polygonal model d_{14}–d_{15}–d_{19} is created, and instead of

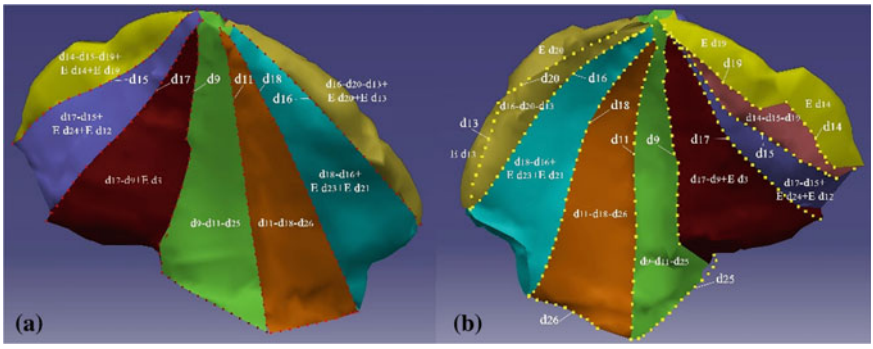

Fig. 5.5 Polygonal models obtained by aggregating parametric regions and parts of edges **a** outer side, **b** inner side

polygonal model d_{16}–d_{20}–$d_{13} + Ed_{20} + Ed_{13}$ polygonal model d_{16}–d_{20}–d_{13}, since the parts which describe the upper edge of the hip bone were constructed in the previous step. Aggregated regions at the inner side are presented in Fig. 5.5b where the yellow dots show the boundaries of the resulting polygonal models corresponding to the curves through parameters.

Individual polygonal models of aggregated regions were merged into a single polygonal model, which required some additional improvement near the most superior point on the iliac crest (point 1). After cleaning (editing convex and concave triangles, detecting and editing collision triangles) and smoothing, the optimization of the polygonal model was performed. The analysis of the model was performed by comparing the initial polygonal model of the ilium wing (obtained from CT images) with the obtained model, where the deviation and distances were measured.

Deviations were measured between the initial polygonal model (reference model) and the model obtained by aggregating regions and parts of the edges (the model to measure). Maximal positive deviation was 10 mm, maximal negative deviation was −9.97 mm, expressed in the area around the posterior superior iliac spine (PSIS), around the posterior gluteal line (in her upper part) and just above parameter d_{26}, while 88.69% of the model surface had the deviations in the amount from −6.65 to 6.67 mm. Deviation analysis is presented in Fig. 5.6.

Distance analysis between the initial polygonal model, obtained from CT images (Source) and the polygonal model obtained by aggregating of the regions (Target)

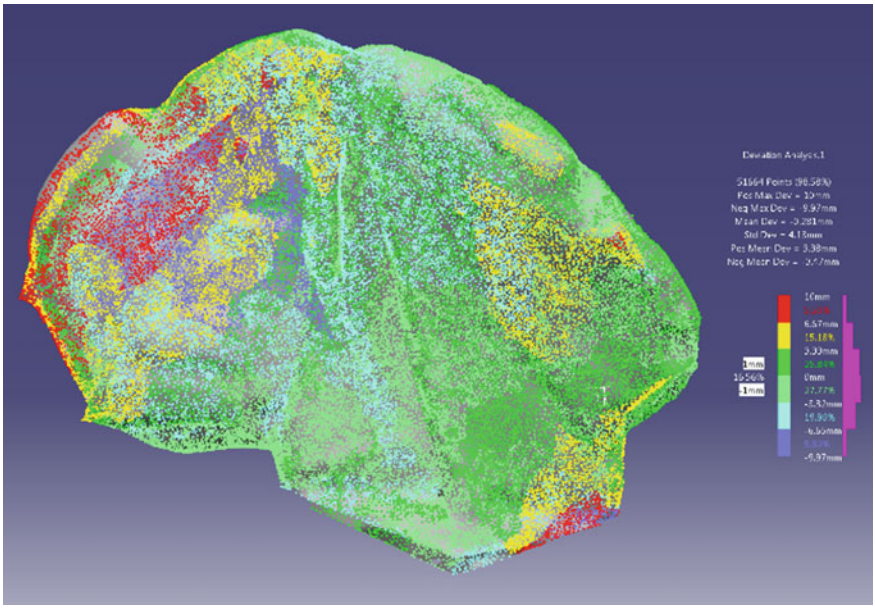

Fig. 5.6 Analysis of deviations between the initial and polygonal model obtained by aggregating regions

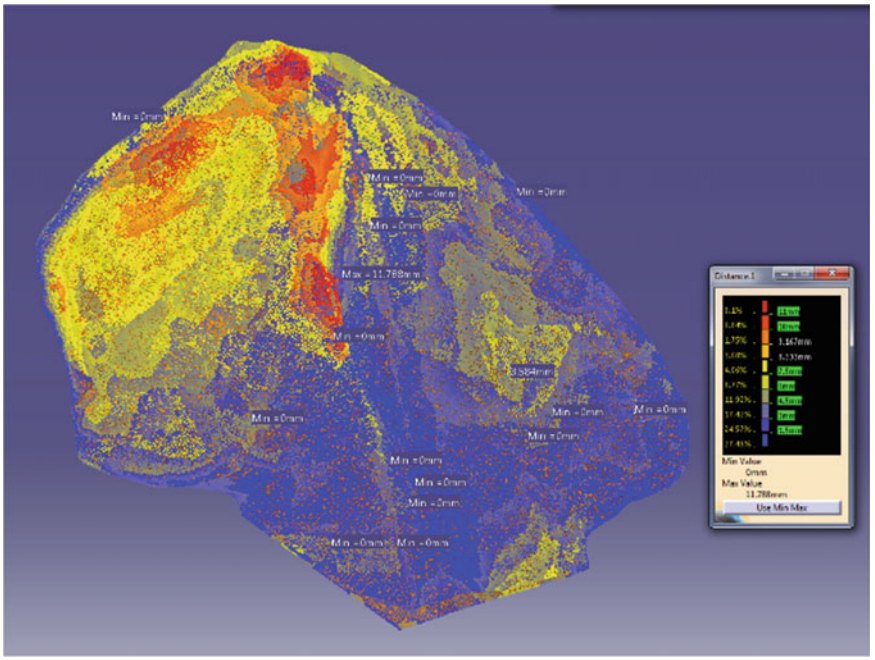

Fig. 5.7 Distance analysis between the outer sides of initial polygonal model and the polygonal model obtained by aggregating parametric regions

was performed with an accuracy of 0.001 mm and shown in the form of a color coded map in Fig. 5.7 and 5.8. Normal distances were taken for measurement direction. At the outer side of the bone maximum distance was pronounced in the middle part of the wing (below point 1), above parameter d_{11} (presented by red color in Fig. 5.7), with the value of 11.788 mm.

At the inner side maximal distance was just below the superior edge, at the auricular surface and in the area which is located left from auricular surface (presented by red color in Fig. 5.8).

5.3.2 Comparative Analysis of the Obtained Models

The comparison of the obtained polygonal models was performed based on the results acquired by the analysis of geometry, deviations and distances (deviations) between the initial and the obtained models. The first model was created without using the method of parametric regions, the second involved using method of parametric regions and the third using the method of parametric regions with aggregating regions.

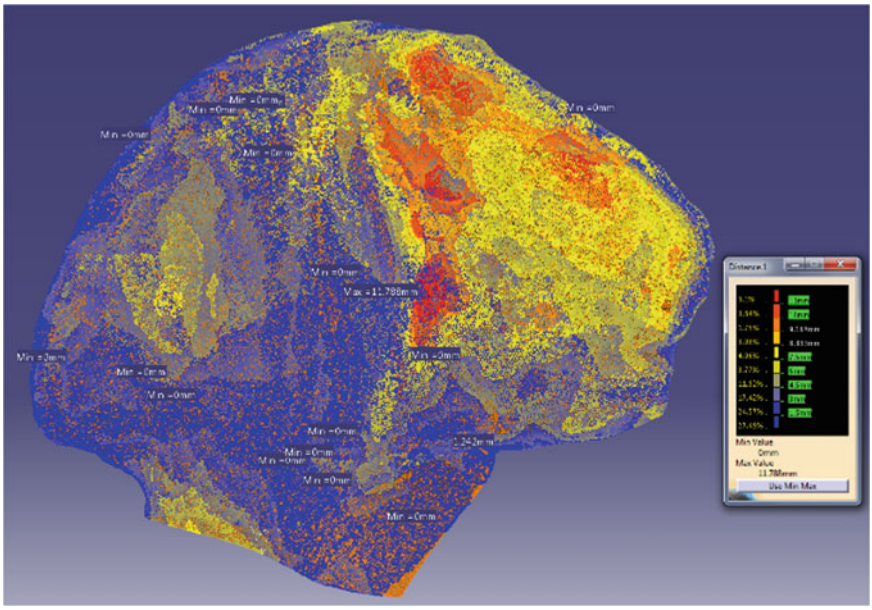

Fig. 5.8 Distance analysis between the inner sides of initial polygonal model and the polygonal model obtained by aggregating parametric regions

The parameters chosen for geometry analysis are Neighborhood values (the maximal edge length of the triangles displayed) before and after model optimization, statistical indicators such as number of points and triangles, the need for editing triangles and the existence of holes which need to be filled. In order to compare the models, optimization was conducted using the same parameter's values in all cases (minimal length 0.5 mm, maximal length 1 mm and the values of dihedral angle 30°). Comparative geometry analysis according to chosen parameters is presented in Table 5.5, where PM stands for polygonal model.

The second polygonal model gives the best results considering the need for editing triangles and filling holes. This model is the easiest to optimize in one step with the ratio of optimization of 6.067, calculated as the ratio of the maximal edge lengths

Table 5.5 Comparative geometry analysis. Expanded from Trajanovic et al. (2018)

Polygonal model parameters	The first PM	The second PM	The third PM
Neighborhood before optimization (mm)	18.599	11.394	9.921
Neighborhood after optimization (mm)	2.41	1.878	3.105
Number of points	1354	2421	2220
Number of triangles	2610	4808	3721
Triangles editing	Yes	No	Yes
Holes existence	Yes	No	Yes

Table 5.6 Comparative analysis for deviation parameters. Expanded from Trajanovic et al. (2018)

Deviation parameters	The first PM	The second PM	The third PM
Positive maximal deviation (mm)	11.7	12	10
Negative maximal deviation (mm)	−10.7	−10.1	−9.97
Mean deviation (mm)	0.567	−0.276	−0.281
Standard deviation (mm)	4.03	4.29	4.13
Positive mean deviation (mm)	3.58	3.49	3.38
Negative mean deviation (mm)	−2.76	−3.54	−3.47
Part of model surface with deviation values from −1 to 1 mm (%)	22.69	16.98	16.56

of the triangles, and very low neighborhood value, which sequentially leads to the largest number of triangles, comparing with the first and the third polygonal model.

The values of positive maximal and negative deviation, mean and standard deviation, positive and negative mean deviation, expressed in millimeters are taken into account for deviation analysis. The part of the model surface expressed in % where the value of deviation is in the range from −1 to 1 mm, used as the common denominator for all three analyzes, is also presented. The above values are presented in Table 5.6, where PM stands for polygonal model.

The third model has the smallest deviation regarding the initial polygonal model, if we consider the values for positive maximum and minimum deviation and positive mean deviation. On the other side, the mean deviation is the lowest in the second model, while the first model shows the best characteristics based on the values of the negative mean deviation and the area of the model that has a small value of deviations.

Statistical data from color coded maps with the same scale gradients were used for comparative distance analysis between the initial polygonal model and obtained polygonal model. Distance values were ranged in four classes and the cumulative values for the parts of the surface model expressed in %, found within the appropriate tolerance limits are presented in Table 5.7 (PM stands for polygonal model).

Table 5.7 Comparative analysis for distance values. Expanded from Trajanovic et al. (2018)

Distance values (mm)	The first PM	The second PM	The third PM
	Model surface (%)		
0–3	51.75	50.41	52.06
0–4.5	69.46	68.77	69.48
0–6	81.12	79.42	81.40
0–10	96.76	98.34	99.06
	Maximum distance (mm)		
	14.238	12.243	11.788

Taking into account the values shown in Table 5.6 by the criteria of deviation values for the given ranges, as well as for the maximum deviation value, the third model should be preferred over the previous two because the values for the model area expressed in % are the largest for all ranges given in Table 5.7. This statement, along with the fact that the third model has the smallest deviation value, leads to the conclusion that the third model is actually the one that deviates the least from the initial model.

Considering the results of comparative analyses of geometry, deviations and distances, and especially taking into account the fact that the second model is the only one that does not require additional editing of the obtained surfaces, has the best mean deviation, and that the difference in surfaces is in the range of 0–10 mm insignificant in relation to the third model (0.72%), as well as the difference in the maximum deviation values between the second and third model 0.635 mm, the second model should be chosen for the construction of the polygonal model of the complete wing of ilium. Additional argument for this is the fact that the difference in the areas of the model where the deviations range from −1 to 1 mm is only 0.42% in favor of the third model, but the time required to obtain the second model is significantly shorter. But, in the cases where there is a need to create some of the individual parts of the wing of ilium the third model should be used as a better solution.

5.3.3 Application of the Method of Parametric Regions for Implant Creation

An additional aspect of the application of the method of parametric regions lies in the fact that individual regions can be divided into subregions, in accordance with the needs, i.e., the parts of the bone for which it is necessary to make an personalized implant.

These implants can be made of artificial materials (substitutes for bone material) or natural bone in the form of an allograph obtained from a donor or in the form of an autograph of bone taken from a healthy part of the bone or from the patient's skeletal system. Thanks to the development of biomaterials, a large number of different materials, such as metals, polymers, ceramics and composites are successfully used for bone repair. In any case, there are always problems when creating an implant of the appropriate shape from the chosen material. In orthopedics, the geometry of a personalized implant is hand-drawn, and such implants can have geometric errors that make them less effective for a longer period of time. With the development of CAD, CAE (Computer Aided Engineering), CAD/CAM (Computer Aided Design/Computer Aided Manufacturing), new trends in medical technology are emerging that lead to a personalized approach, i.e., enable the construction and production of personalized implants at an affordable price and within a reasonable time (Trajanovic and Tufegdzic 2018).

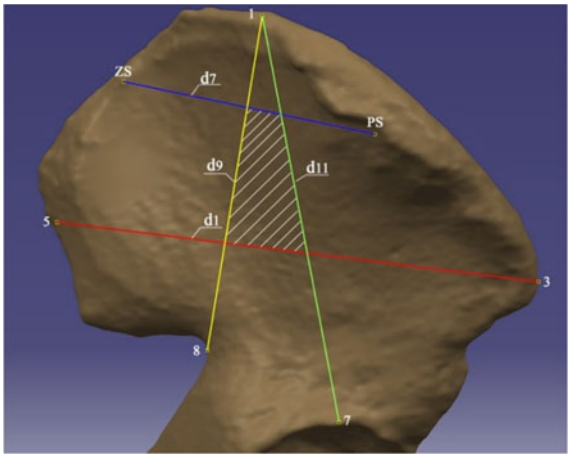

Fig. 5.9 Part of the parametric region d_9–d_{11}

In the example of applying the method of parametric regions it will be assumed that the bone damage is in the area at the outer side of the wing of ilium, in the parametric region d_9–d_{11}, bounded by parameters d_7 and d_1, which corresponds to the hatched area in Fig. 5.9. The first step was to determine anatomical landmarks 1, 3, 5 and 8, since the values for the parameters d_1 and d_9 need to be measured and inserted into Excel sheet, while the values for the parameters d_7 and d_{11} were calculated according to the formulas in Table 5.3 (which already exist in the Excel file). Points at the parameters d_1, d_9, d_7 and d_{11} were selected from special sheets. Point coordinates were calculated according to the algorithm used for the ilium bone, based on the regression equations which also exist in the Excel file, and selected by running a macro for point selection. The selected point coordinates must satisfy the condition from expression for N_c. In this case, only the points at the outer side should be selected (indexed with $d_{i\text{-}j\text{-}01}$). This procedure is repeated after selecting the required region, in this case d_9–d_{11}.

The values for the point coordinates are exported to the CAD program. Points that do not belong to the target area should be removed manually. These are all points outside the area bound by the points at the parameters d_7 and d_1, as well as the points at d_9 and d_{11}. After removing the unnecessary points, the remaining points are converted into a point cloud, and finally the desired subregion polygonal surface is created.

In order to conduct the analysis of deviations and distances the initial subregion polygonal surface is created by cutting the initial polygonal model of wing of ilium, obtained from CT images. Deviations were measured between the initial subregion polygonal model and the obtained subregion polygonal surface. Most of the obtained polygonal surface (71.73%) has deviations from the initial model in the range of −3.31 to 2.67 mm. The value for maximal positive deviation is 4 mm and the maximal negative deviation is −4.96 mm.

A slight maximum deviation of the constructed polygonal surface is noticeable, i.e., 1.36%. Maximal distance value is 4.649 mm. Most of the obtained subregion polygonal surface (89.22%) is within the tolerance limits from 0 to 2.905 mm. The obtained surface can be additionally adjusted in the procedures of successive iterations, which imply the possibility of removing additional points or small corrections of coordinate values.

Methodology applied in creating the part of the area bound by parameters can be applied to each of the regions or subregions. Subregions can be selected depending on the part of the bone that needs to be created, grouped or further divided. It is necessary to determine only the landmarks used to define the parameters whose values are to be measured, from two planar X-ray projections. Created subregions polygonal models can be increased or decreased using the offset function in CAD program.

The required subregion can also be constructed by intersecting a given parametric region. In the presented example, it is necessary to construct a complete parametric region d_9–d_{11} first, which is further intersected by the curves obtained by cutting polygonal models with planes determined by the given parameters d_7 and d_1.

The results of the deviation analysis between initial subregion polygonal model and obtained subregion polygonal model show that 67.37% of the subregion surface area of the obtained model is in the range of deviations −2.99 to 2.76 mm. On the other hand, the distance analysis gives better results compared to the method of separating points in the area of interest, because 91.39% of the obtained model surface is within the tolerance limits from 0 to 0.512 mm, and the value of the maximum deviation is reduced to 4.092 mm.

The methodology can also be applied to obtain polygonal models with completely arbitrary shape, but it is necessary to have a CT image since the target areas cannot be localized with sufficient accuracy from two plane X-ray projections.

5.3.4 Parametric Regions at the Ischium and Pubic Bone

The parametric region separation method described above at the example at the wing of ilium bone can be used to create 3D models of the ischium and pubic bones, or its parts. In some areas, it is necessary to use some of the parameters that are previously defined at the ilium bone, such as d_{25} and d_{26} (Fig. 5.2), and some of the anatomical landmarks defined for the wing of ilium, 4, 7 and 8 (Fig. 5.1). In such manner, a connection between constitutive entities of the hip bone is established, which ultimately provides complete coverage of the hip bone surface.

Input data in the form of parameters were also acquired from A-P and lateral X-ray projection of the hip bones. From the ischium bone the values for 7 parameters (d_{27}, d_{32}, d_{38}, d_{40}, d_{41}, d_{42} and d_{45}) and from pubic bone the values for 4 parameters (d_{47}, d_{48}, d_{49} and d_{57}) were taken. Predicted parameters' values were calculated using regression equations presented in Table 5.3. Parameters are used to obtain intersections with polygonal bone models from the sample using Quick Plane

Definition function in CATIA module. To determine the points at the intersection curves, cross-sections of polygonal models with planes at distances of 4 mm that are perpendicular to the parameters should be used. Two cross-sectional points are to be found on each of these curves. The notation for these points should be the same as in the case of ilium bone, $d_{i\text{-}j\text{-}01}$ and $d_{i\text{-}j\text{-}02}$ (index i refers the number of parameter, index j refers to the ordinal number of the curve obtained by intersecting with the plane perpendicular to the parameter, index 01 shows that the point is on the outer side, index 02 shows that the point is at the inner side of the hip bone). After measuring points' coordinates, values will be statistically processed. Testing and regression models will be selected for each of the points in the manner described for the points at the surface of the wing of ilium bone.

After that, the regionalization of the surfaces which describe the body of the ischium bone and the ramus of ischium, as well as the body and superior and inferior ramus of the pubic bone should be done, assigning the same notation for the labels according to parameters that represent boundaries for given region, as it was in the case of parametric regions at the wing of ilium bone.

At the ischium bone it is necessary to separate the following parametric regions:

1. Parametric region d_{27}–d_{28}—region outlined by the parameters d_{27}, d_{28} and with the part of the posterior edge between the points 8 and 15
2. Parametric region d_{28}–d_{29}–d_{30}—region whose boundaries are parameters d_{28}, d_{29} and d_{30}
3. Parametric region d_{30}–d_{31}—region outlined by the parameters d_{30}, d_{31} and with a part of the posterior edge between points 16 and 17
4. Parametric region d_{31}–d_{32}–d_{33}—region whose boundaries are parameters d_{31}, d_{32} and d_{33}
5. Parametric region d_{32}–d_{34}–d_{36}—region whose boundaries are parameters d_{32}, d_{34} and d_{36}
6. Parametric region d_{36}–d_{37}–$LAc_{12\text{–}14}$—region outlined by the parameters d_{36}, d_{37}, and with part of acetabular rim between points 12 and 14
7. Parametric region d_{34}–d_{35}–d_{38}—region whose boundaries are parameters d_{34}, d_{35} and d_{38}
8. Parametric region d_{37}–d_{38}–d_{39}—region whose boundaries are parameters d_{37}, d_{38} and d_{39}
9. Parametric region d_{39}–d_{40}—region outlined by the parameters d_{39}, d_{40}, and with the part of the rim of the obturator foramen, between the projections of point 14 on the rim of the obturator foramen and point 21
10. Parametric region d_{40}–d_{41}–d_{42}—region whose boundaries are parameters d_{40}, d_{41} and d_{42}
11. Parametric region d_{42}–d_{43}—region outlined by the parameters d_{42}, d_{43}, and with the part of rim of the obturator foramen, between the points 21 and 22
12. Parametric region d_{43}–d_{44}–d_{45}—region whose boundaries are parameters d_{43}, d_{44} and d_{45}.

For a detailed description of the ischium bone geometry, it is necessary to define the parts of the polygonal model that describe the edges and part of the ischial

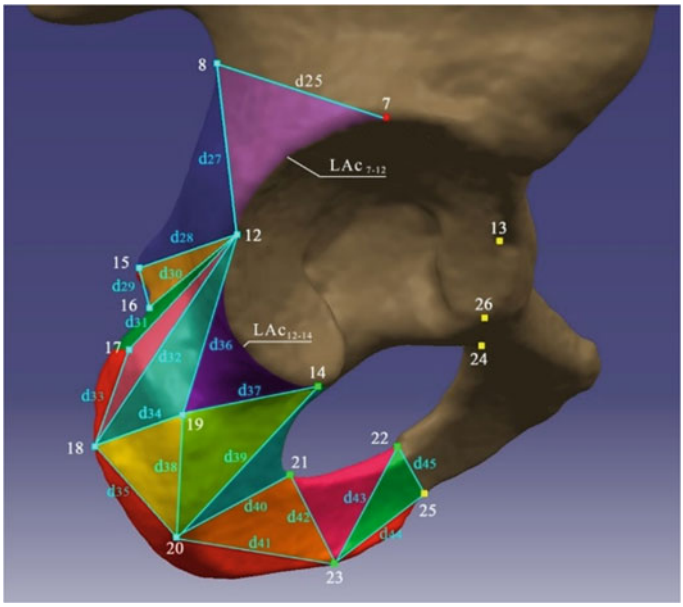

Fig. 5.10 Parametric regions and the parts of the hip bone edges at the ischium bone

tuberosity. The part of the posterior edge which is not covered by above regions is described by the part of the polygonal model left of the parameter d_{29}. The parts of the ischial tuberosity are described by the parts of the polygonal model left from the parameter d_{33} and left and below the parameter d_{35}, while the part of the inferior edge of the hip bone is described by the parts of the polygonal model below the parameters d_{41} and d_{44}. These parts are represented by the red color in Fig. 5.10 together with parametric regions at the ischium bone. To determine and predict the coordinates of the points on these parts of the polygonal model, the methodology described for the wing of ilium bone will be used, where the parts of the polygonal model are intersected by curves that are perpendicular to the aforementioned parameters.

Since the methodology for creating a surface model of the pubic bone is exactly the same, the parametric regions will be listed below. In order to fully describe the pubic bone geometry, the parts of the polygonal model which correspond to the superior and inferior edge parts will also be presented.

The selected parametric regions at the pubic bone (see Fig. 5.11) are:

1. Parametric region d_{45}–d_{46}–d_{47}, region whose boundaries are parameters d_{45}, d_{46} and d_{47}
2. Parametric region d_{47}–d_{48}–d_{49}, region whose boundaries are parameters d_{47}, d_{48} and d_{49}
3. Parametric region d_{49}–d_{50}–d_{51}, region whose boundaries are parameters d_{49}, d_{50} and d_{51}

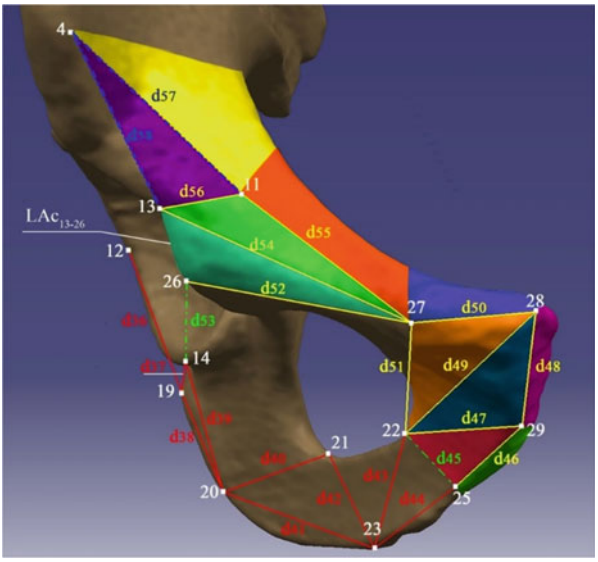

Fig. 5.11 Parametric regions and the parts of the hip bone edges at the pubic bone

4. Parametric region d_{52}–d_{54}—$LAc_{13–26}$, region outlined by the parameters d_{52}, d_{54} and with part of acetabular rim between points 13 and 26
5. Parametric region d_{54}–d_{55}–d_{56}—region outlined by the parameters d_{54}, d_{55} and d_{56}.

The parts of the inferior edge that are included in following parts of the polygonal model are located below and right from the parameter d_{46}, right from the parameter d_{48} and above the parameter d_{50}. The surfaces at the part of the superior pubic ramus, so as the part of the corresponding superior edge are described by the points constructed on curves that are perpendicular to the parameter d_{55}. The part of the anterior edge towards point 4, as well as part of the body of the ilium bone, is characterized by the points which belong to the set of curves perpendicular to the parameter d_{58}. At the surface which corresponds to the part of the edge of the obturator foramen, from point 22 toward the superior pubic ramus, it is necessary to use the points situated at the set of curves which are perpendicular to the parameter d_{51}. The surface which corresponds to the part of the edge of the obturator foramen below the acetabular notch is presented by the points at the curves that are perpendicular to the parameter d_{53}. These parts are shown in dark green, blue, orange and yellow in Fig. 5.11.

Beside the parametric regions that include parts of different bones (so called common parametric regions) mentioned and presented above d_{25}–d_{27}–$LAc_{7–12}$ (see Fig. 5.10) and d_{26}–d_{58}–$Lac_{13–26}$ (see Fig. 5.11 for $Lac_{13–26}$), it is necessary to point out the parametric region d_{56}–d_{57}–d_{58}. It is a region outlined by the parameters d_{56}, d_{57}, and d_{58} and curves perpendicular to the parameter d_{57} will be used to obtain additional points.

5.4 Conclusion

The method of parametric regions enables reverse engineering of the hip bone, with sufficient accuracy, in a short time. The method can be applied in case of complete or incomplete volumetric data, which can occur due to trauma, osteoporosis or tumors, but also in cases when the only data sources are 2D X-rays in the A-P and lateral projection. The implementation of parameter-based approach allows subject specific morphometry of the hip bone, using 34 anatomical landmarks, interconnected by 58 straight lines which represent parameters. On the other hand, complete morphometry is provided by 21 measured values of the parameters from 2D X-rays, due to developed statistical regression models which establish proper dependencies between parameters.

Measured and calculated parameters' values are used to predict numerical values for coordinates of the points on the surface at the wing of ilium bone, based on mathematical models. These points are defined for each of the 10 parametric regions, as well as for the corresponding edges. By selecting all points in the region, or some of them, it is possible to construct a polygonal model of the whole region or its parts. Depending on the needs and parts of the polygonal model of the wing of ilium bone that need to be constructed, it is possible to combine and merge individual parameter regions and parts of the edges, only at the outer or at the inner side of the bone, or on both sides at the same time.

Parametric regions are separated at the other constitutive bones, such as 12 regions at the ischium bone, 5 regions at the pubic bone and 3 common regions, since they are outlined by parameters which connect landmarks at different bones. The parts of the polygonal model which describe corresponding edges, the part of the ischial tuberosity and the part of the pubic body, are also defined. These regions and parts of the bones impose certain directions of further research in order to find the regression equations of the coordinates of points on the parameters, edges and parametric regions.

References

Aguirre MR, Linguraru MG, Ballester MAG (2007) Statistical bone shape analysis for image free surgery. Acta Univ Cibiniensis Tech Ser LV:121–129. https://doi.org/10.7892/boris.61086

Angelopoulou A, Psarrou A, Rodríguez JG et al (2015) 3D reconstruction of medical images from slices automatically landmarked with growing neural models. Neurocomputing 150(A):16–25. https://doi.org/10.1016/j.neucom.2014.03.078

Baka N, Niessen WJ, Kaptein BL et al (2010) Correspondence free 3D statistical shape model fitting to sparse X-ray projections. In: Davant BM, Haynor DR (eds) Proceedings of SPIE 7623. Medical imaging 2010: image processing, vol 7623. San Diego, California, United States, 76230D-1. https://doi.org/10.1117/12.840935

Benameur S, Mignotte M, Parent S et al (2001) 3D biplanar reconstruction of scoliotic vertebrae using statistical models. In: Proceedings of the 2001 IEEE computer society conference

on computer vision and pattern recognition, CVPR 2001, vol 2. Kauai, HI, USA, pp 577–582. https://doi.org/10.1109/CVPR.2001.991014

Besbes A (2010) Image segmentation using MRFs and statistical shape modeling. Dissertation, Ecole Centrale Paris, Paris

Betti L, Cramon-Taubadel N, Manica A et al (2013) Global geometric morphometric analyses of the human pelvis reveal substantial neutral population history effects, even across sexes. PLoS ONE 8(2):e55909. https://doi.org/10.1371/journal.pone.0055909

Blanc R, Seiler C, Székely G et al (2012) Statistical model based shape prediction from a combination of direct observations and various surrogates: application to orthopaedic research. Med Image Anal 16(6):1156–1166. https://doi.org/10.1016/j.media.2012.04.004

Boulay C, Tardieu C, Benaim C et al (2006) Three-dimensional study of pelvic asymmetry on anatomical specimens and its clinical perspectives. J Anat 208(1):21–33. https://doi.org/10.1111/j.1469-7580.2006.00513.x

Chen JH, Shapiro LG (2009) 3D point correspondence by minimum description length with 2DPCA. In: Proceedings of annual international conference of the IEEE, 3–6 Sept 2009. Engineering in Medicine and Biology Society, Minneapolis, MN, USA, pp 5657–5660. https://doi.org/10.1109/IEMBS.2009.5333769

Chintalapani G, Ellingsen LM, Sadowsky O et al (2007) Statistical atlases of bone anatomy: construction, iterative improvement and validation. In: Ayache N, Ourselin S, Maeder A (eds) Medical image computing and computer-assisted intervention—MICCAI 2007. MICCAI 2007. Lecture notes in computer science, vol 4791. Springer, Berlin, Heidelberg. pp 499–506. https://doi.org/10.1007/978-3-540-75757-3_61

Decker S (2010) The human in 3D: advanced morphometric analysis of high-resolution anatomically accurate computed models. Dissertation, College of Medicine, University of South Florida, Tampa, USA

Dhindsa G, Singh P, Singh Z (2013) Morphometry of the adult human dry hip bone. Int J Pharm Pharm Sci 5(2):505–507

Ehlke M, Ramm H, Lamecker H et al (2013) Fast generation of virtual X-ray images for reconstruction of 3D anatomy. IEEE Trans vis Comput Graph 19(12):2673–2682. https://doi.org/10.1109/TVCG.2013.159

Fattah EDHAA (2013) Reconstruction of patient-specific bone models from X-ray radiography. Dissertation, University of Tennessee, Knoxville

Gupta S, Vaghela B, Dave M (2014) Morphometric analysis of pubic bone in sex dimorphism. Int J Sci Res 3(1):381–383. https://doi.org/10.36106/ijsr

Kirschner M (2013) The probabilistic active shape model: from model construction to flexible medical image segmentation. Dissertation, Fachbereich Informatik der Technischen Universität, Darmstadt

Lamecker H, Seebass M, Hege HC et al (2004) A 3D statistical shape model of the pelvis bone for segmentation. In: Fitzpatrick JM, Sonka M (eds) Proceedings of SPIE 5370. Medical imaging 2004: image processing, vol 5370. San Diego, California, United States, pp 1341–1351. https://doi.org/10.1117/12.534145

Lamecker H, Wenckebach TH, Hege HC (2006) Atlas-based 3D-shape reconstruction from X-ray images. In: Proceedings of the International Conference of Pattern Recognition, vol. I. IEEE Computer Society, Hong Kong, China, pp 371–374. https://doi.org/10.1109/ICPR.2006.279

Lamecker H (2008) Variational and statistical shape modeling for 3D geometry reconstruction. Dissertation, Fachbereich Mathematik und Informatik der Freien Universität Berlin, Berlin

Lubovsky O, Peleg E, Joskowicz L et al (2010) Acetabular orientation variability and symmetry based on CT scans of adults. Int J Comput Assist Radiol Surg 5(5):449–454. https://doi.org/10.1007/s11548-010-0521-9

Margam S, Doshi M, Jadhav S et al (2013) Sex and side determination of human hip bone by metric parameters of its posterior border. Natl J Clin Anat 2(1):16–21

O'Connell L (2004) An initial evaluation of the relationship between human pelvic size and shape and the distribution, type and severity of vertebral degenerative disease in archaeological material (Volume 1). Disseratation, Bournemouth University, Bournemouth, United Kingdom

Okoseimiema A, Udoaka A (2013) Radiologic determination of ischiopubic index in South-South Nigerian population. Asian J Med Sci 5(5):96–100. https://doi.org/10.19026/ajms.5.5361

Phillips ATM, Pankaj P, Howie CR et al (2007) Finite element modelling of the pelvis: inclusion of muscular and ligamentous boundary conditions. Med Eng Phys 29(7):739–748. https://doi.org/10.1016/j.medengphy.2006.08.010

Popov I, Onuh SO (2009) Reverse engineering of pelvic bone for hip joint replacement. J Med Eng Technol 33(6):454–459. https://doi.org/10.1080/03091900902952634

Ruiz LMA (2005) Reconstruction 3D du bassin humain à partir d'images médicales multimodales incomplètes. Application à l'assistance de la chirurgie de la prothèse totale de la hanche (PTH). Dissertation, Institut National Polytechnique de Grenoble—INPG, Français

Seim H, Kainmueller D, Heller M et al (2008) Automatic segmentation of the pelvic bones from CT data based on a statistical shape model. In: Botha CP, Kindlmann G, Niessen WJ et al (eds) EG VCBM'08: Proceedings of the first Eurographics conference on visual computing for biomedicine, Eurographics workshop on visual computing for biomedicine, 6–7 October 2008. Eurographics Association, Delft, Netherlands, pp 93–100

Sharma G, Vijayvergiya T (2013) Evaluation the various criteria of sex determination of hip bone of Jhalawar region of Rajasthan. J Pharm Biomed Sci 26(26):330–335

Shim VB, Pitto RP, Streicher RM et al (2007) The use of sparse CT datasets for auto-generating accurate FE models of the femur and pelvis. J Biomech 40(1):26–35. https://doi.org/10.1016/j.jbiomech.2005.11.018

Sierra R, Zsemlye G, Székely G et al (2006) Generation of variable anatomical models for surgical training simulators. Med Image Anal 10:275–285. https://doi.org/10.1016/j.media.2005.11.003

Styner MA, Rajamani KT, Nolte LP et al (2003) Evaluation of 3D correspondence methods for model building. In: Taylor C, Noble JA (eds) Information processing in medical imaging. IPMI 2003. Lecture notes in computer science, vol 2732. Springer, Berlin, Heidelberg, pp 63–75. https://doi.org/10.1007/978-3-540-45087-0_6

Su GM, Lai YC, Kwasinski A et al (2013) 3D visual communications. Wiley, Chichester West, United Kingdom

Trajanovic M, Tufegdzic M, Arsic S (2018) Obtaining patient-specific point model of the human ilium bone in the case of incomplete volumetric data using the method of parametric regions. Australas Phys Eng Sci Med 41:931–944. https://doi.org/10.1007/s13246-018-0689-9

Trajanovic M, Tufegdzic M (2018) Trends in producing personalized bone implants using additive manufacturing. In: Doroslovački R (ed) Proceedings of 13th international scientific conference. MMA 2018, September 28–29, 2018. Flexible Technologies, Novi Sad, Serbia, pp 371–373

Tufegdžić M, Trajanović M, Arsić S et al (2013) Toward reverse engineering of the hip bone. In: Proceedings of the 35th International conference on production Engineering, ICPE 2013. Faculty of Mechanical and Civil Engineering in Kraljevo, Department of Production Technologies, Kraljevo-Kopaonik, Serbia, September 25–28, 2013, pp 319–324

Tufegdzic M, Arsic S, Trajanovic M (2015) Parameter-based morphometry of the wing of ilium. J Anat Soc India 64(2):129–135. https://doi.org/10.1016/j.jasi.2015.10.008

Yaoa J, Taylor R (2012) Deformable 2D–3D medical image registration using a statistical model: accuracy factor assessment. Am J Sci Eng 1(2):1–13

Zheng G (2009) Statistical deformable model-based reconstruction of a patient-specific surface model from single standard X-ray radiograph. Comput Anal Images Patterns 57(2):672–679. https://doi.org/10.1118/1.3327453

Zsemlye G (2005) Shape prediction from partial information. Dissertation, Swiss Federal Institute of Technology, Zurich